

Inner ear biomechanics reveals Late Triassic origin of mammalian endothermy

Ricardo Araujo (✉ paradoxides@gmail.com)

Instituto de Plasmas e Fusão Nuclear, Instituto Superior Técnico, Universidade de Lisboa

<https://orcid.org/0000-0001-5058-2983>

Romain David (✉ r.david@nhm.ac.uk)

The Natural History Museum

Julien Benoit

University of the Witwatersrand <https://orcid.org/0000-0001-5378-3940>

Lungmus Jacqueline

University of Chicago

Fred Spoor

Centre for Human Evolution Research, Department of Earth Sciences <https://orcid.org/0000-0002-8829-7421>

Alexander Stoessel

Friedrich-Schiller-Universität Jena Institut für Zoologie und Evolutionsforschung mit Phyletischem Museum

Paul Barrett

The Natural History Museum <https://orcid.org/0000-0003-0412-3000>

Jessica Maisano

The University of Texas Austin

Eric Ekdale

San Diego State University

Maeva Orliac

Institut des Sciences de l'Evolution de Montpellier, Université de Montpellier

Zhe-Xi Luo

The University of Chicago <https://orcid.org/0000-0003-2170-8879>

Agustin Martinelli

Museo Argentino de Ciencias Naturales <https://orcid.org/0000-0003-4489-0888>

Eva Hoffman

American Museum of Natural History

Christian Sidor

University of Washington

Rui Martins

Instituto de Plasmas e Fusão Nuclear, Instituto Superior Técnico, Universidade de Lisboa

Kenneth Angielczyk (✉ kangielczyk@fieldmuseum.org)

The Field Museum

Biological Sciences - Article

Keywords: mammalian endothermy, inner ear, morphological changes

Posted Date: June 2nd, 2021

DOI: <https://doi.org/10.21203/rs.3.rs-570966/v1>

License:   This work is licensed under a Creative Commons Attribution 4.0 International License.

[Read Full License](#)

Version of Record: A version of this preprint was published at Nature on July 20th, 2022. See the published version at <https://doi.org/10.1038/s41586-022-04963-z>.

Abstract

Endothermy (“warm-bloodedness”) underpins the ecological dominance of mammals and birds in diverse environmental settings¹⁻³. However, it is unclear when this crucial feature emerged during mammalian evolutionary history, as most fossil evidence is ambiguous⁴⁻²⁵. Here, we show that new information on this key evolutionary transition can be obtained from the morphology of the endolymph-filled semicircular ducts of the inner ear that monitor head rotations and are essential for motor coordination, navigation, and spatial awareness²⁶⁻³¹. Increased body temperature during the ectotherm–endotherm transition of mammal ancestors would decrease endolymph viscosity, negatively impacting the biomechanics of the semicircular ducts^{32,33}, while simultaneously increasing activity levels^{34,35} required improved performance³⁶. Specific morphological changes to the membranous ducts and enclosing bony canals were, therefore, necessary to maintain optimal functionality. We track these morphological changes in 341 vertebrates, including 56 extinct synapsids, and show that canals with relatively thin cross-sections and small radii of curvature are indicative of mammalian endothermy. This inner ear morphotype evolved abruptly ~233 million years ago, during the Late Triassic, in Mammaliamorpha. Our conclusion differs from previous suggestions³⁻¹⁷, and we interpret most stem-mammals as ectotherms. Endothermy as a crucial physiological characteristic joins other distinctive mammalian features that arose during this period of climatic instability³⁷⁻³⁹.

*Ricardo Araújo and Romain David contributed equally to this work.

Main Text

Endotherms can maintain high and nearly constant body temperature through metabolic heat production, allowing them to optimize chemical reactions and sustain aerobic activity for long periods of time while remaining relatively independent from external conditions^{1,2,40}. Compared to ectotherms, endotherms are more active, travel farther, and achieve higher locomotor speeds, all at the expense of higher energy costs^{34,35} (Supplementary Data 1). Consequently, extant mammals and birds occupy a variety of ecological niches unrivalled by other vertebrates. Endothermy is a quintessentially mammalian feature, intimately related to other hallmarks such as lactation, sweat glands and fur^{2,3}. However, its evolution remains one of the great unsolved mysteries of palaeontology^{2,3}. Lines of evidence invoked to identify the emergence of mammalian endothermy rely mostly on skeletal anatomical features, but also on ichnological, histological and isotopic information, which have been used as correlates for aerobic capacity^{4,5,8,10,24}, basal metabolic rate^{7,9,23,11-13}, thermal insulation^{6,14,22}, parental care¹⁵, nocturnality²¹ and body temperature^{16,20,25}. Most of these features are poorly sampled in the fossil record, not linked directly to body temperature and often cannot be interpreted as unambiguous markers for endothermy without confounding factors. In addition, the origins of many of these features date back to the Permo-Triassic mass extinction, but others originated iteratively throughout the Triassic^{7,19,20,22}, making it difficult to pinpoint the origin of mammalian endothermy.

Here we show that the functional morphology of the semicircular duct system of the inner ear (SDS) provides new and independent insights that help solve this problem. Semicircular ducts monitor head rotation and are filled with a fluid called endolymph, whose viscosity affects function and depends on body temperature^{32,33}. Head motion proprioception is essential for navigation²⁹, balance⁴¹, vision²⁸, motor coordination³⁰, and spatial awareness³¹. Therefore, the SDS is expected to attune to the spectrum of head rotations experienced by an organism³⁶. In this context, endotherms not only need to compensate for the decreased response speed induced by the less viscous endolymph associated with elevated body temperature^{32,33}, they also require a more efficient SDS than ectotherms, because they are more active on average^{34,35}. Optimal SDS function can be achieved by modifying endolymph chemistry to increase its viscosity and/or by modifying SDS morphology. To track these adaptations in the fossil record we newly devised the Thermo-Motility Index (TMI), which covaries with both body temperature and overall head motion. This unitless index consists of a biomechanically informed combination of functionally-relevant morphometric parameters of the bony semicircular canals that enclose the SDS (bony part of the index), relevant morphological information about the SDS that cannot be estimated from the canals (membranous-only part of the index) and physicochemical properties of the endolymph (endolymph part of the index) (Methods; Supplementary Methods).

The bony part of the TMI is composed of morphological parameters, measured on the semicircular canals of 362 specimens (Fig. 1, Extended Data Fig. 1, 2). Mammals show the lowest values for relative cross-section thickness and relative radius of curvature (Extended Data Fig. 3), which mostly determine the TMI in tetrapods (Extended Data Table 1). The membranous-only part of the index was investigated when the SDS could be extracted from 3D models, and for some fish from 2D photographs (Methods). Our results show that the average value of the membranous-only part for the 30 sampled mammalian species (3.56), is similar to both the value estimated at the node of Amniota (3.62) and Diapsida (3.63) (Extended Data Fig. 4a). Properties of the endolymph are only known for 8 species, but inferences can be made. The average value of the endolymph part measured in mammals (-4.57)^{32,33} is close to the value at the root of Euteleostei (-4.53)³², suggesting a similar value for basal amniotes (Extended Data Fig. 4b). These observations strongly suggest that neither values for the membranous-only nor the endolymph parts of the TMI changed drastically between the nodes of Amniota and Mammalia. The combined evidence suggests that in extant mammals it is the relatively thin cross-sections and small radii of curvature of the SC in particular that drive high TMI values. Conversely, birds show semicircular canals with relatively large radii of curvature but relative thin cross-sections that are average for amniotes, resulting in a bony part similar to that of other sauropsids (Extended Data Fig. 3). Therefore, birds responded to endothermy differently than mammals by modifying specific aspects of their membranous labyrinth and the physicochemical properties of their endolymph, as reflected in the values of their membranous-only (3.76) and endolymph⁴² (-4.35) parts. Although body temperature directly influences endolymph viscosity and semicircular duct function (Methods), we only find a significant positive correlation between the TMI and body temperature when group averages are considered, and not individual species values (Phylogenetic Generalized Least Squares Regression, $n_{\text{clades}} = 28$, $p\text{-value} = 9.45$

10^{-11} versus $n_{\text{species}} = 230$, $p\text{-value} = 0.11$). At more inclusive taxonomic levels, body temperature shapes the morphotype of the SDS and explains size differences observed among vertebrates³⁶. At the species level, however, behaviorally-induced head motion seems to overtake body temperature and drives morphological variation. Therefore, the TMI can estimate body temperature more accurately for clades than individual species.

When plotting body temperature against the TMI (Fig. 2), we observe that group averages are distributed along two theoretical curves related to endolymph viscosity. Endotherms are shifted toward higher TMI values. From these observations, the average overall head motion of a clade is positively correlated with body temperature, leading to further increase of the TMI compared to values expected under the theoretical relationship with endolymph viscosity. As a result, the overall head motion of endotherms is expected to be up to three times higher on average than for ectotherms of similar body size. This corollary supports the Aerobic Capacity Model that posits that elevated body temperature in endotherms did not evolve in isolation, but as a consequence of increased aerobic capacity⁴³, which translates into increased behavioural activity. The TMI of extant endotherms is significantly higher than that of extant ectotherms (Phylogenetic ANOVA, $n_{\text{Endotherm}} = 145$, $n_{\text{Ectotherm}} = 132$, $p\text{-value} = 7.80 \cdot 10^{-3}$), confirming that this metric can be used to assess the thermal regime of extinct organisms (Extended Data Fig. 5).

Except for non-mammalian mammaliamorphs (NMM) (Mann-Whitney $U = 529$, $P\text{-value} = 1.12 \cdot 10^{-3}$, $n_{\text{NMM}} = 9$, $n_{\text{lepidosaurs}} = 67$), the TMI of non-mammalian synapsids is never significantly higher than that of lepidosaurs, whereas it is always significantly lower than the TMI of mammals (Table 1). Conversely, the TMI of non-mammalian mammaliamorphs (-0.55) does not differ significantly from that of mammals (Mann-Whitney $U = 209$, $P\text{-value} = 0.082$, $n_{\text{NMM}} = 9$, $n_{\text{mammals}} = 77$) and is intermediate between the TMI measured in *Ornithorhynchus* (-0.60) and *Tachyglossus* (-0.48). As extant monotremes are somewhat dependent on ambient temperatures and utilize hibernation and daily torpor^{40,44}, mammaliamorphs were most likely basoendotherms² with body temperatures of $\sim 34^\circ\text{C}$, low basal metabolic rates, and yet relatively active. The TMI of non-mammalian morph probainognathians (-0.91 for NMP) is significantly lower than non-mammalian mammaliamorphs (Mann-Whitney $U = 0$, $P\text{-value} = 0.019$, $n_{\text{NMM}} = 9$, $n_{\text{NMP}} = 3$). This gives strong statistical support for the emergence of endothermy in mammaliamorphs after their split from other cynodonts.

We fit logistic regressions to the TMI distribution to compute the probabilities of endothermy for each fossil taxon and node (Fig. 3, Extended Data Fig. 6, Extended Data Table 2, 3). Based on these logistic regressions, classification of extant species to the corresponding thermal regime has a cross-validated success rate of 86% when the endothermy cut-off is at $P = 0.5$. Accuracy rises to 96% for the larger clades tested in this study. Maximum likelihood ancestral state reconstruction under Brownian motion shows that the threshold of $P = 0.5$ is crossed at the node subtending *Riograndia* and mammals. However, because the TMI of *Riograndia* indicates an ectothermic regime, congruent with other non-mammalian morph probainognathians, it is more parsimonious to consider the emergence of endothermy in Mammaliamorpha, the clade stemming from the last common ancestor of tritylodontids and

mammals⁴⁵. Therefore, non-mammalian mammalianomorphs are unambiguously classified as endotherms. Conversely, all non-mammalian synapsid groups are unequivocally classified as ectotherms, suggesting that sustained aerobic capacity did not evolve in Synapsida before the Late Triassic (Extended Data Table 4). Therefore, microvascularization⁷, nocturnality¹⁸ and putative parental care¹⁵, probably represent inaccurate proxies for endothermy. The acquisition of endothermy in mammalianomorphs is consistent with a pulse in brain enlargement¹⁹, miniaturization^{2,46}, the development of respiratory turbinates²⁰, the evolution of infraorbital canals (related to the presence of vibrissae²²), and regionalization of the vertebral column⁴⁷.

Our sample of 56 extinct stem-mammals is the largest analysed in the context of mammalian endothermy, underscoring the applicability of our proposed proxy to the fossil record. Our sample overlaps with some taxa analysed in previous studies using stable oxygen isotopes and histologically-inferred metabolic rates that pointed to an origin of mammalian endothermy in basal eucynodonts^{7,16} and, independently, within derived dicynodonts^{13,16}. Our analysis confidently rejects the acquisition of endothermy among these more basal synapsids, and we attribute these discrepancies to the narrow breadth of taxonomic sampling and various confounding factors associated with these approaches. Interpreting results for individual taxa rather than clades can be misleading, because sampling comprehensiveness determines interpretative potential. Among non-mammalianomorph synapsids, only *Cricodon* and *Thrinaxodon* show probabilities that could be in agreement with an endothermic regime (69 and 61%). Nevertheless, their TMI remain lower than the threshold below which 95% of ectotherms fall (Fig. 4), and none of their relatives show a similar pattern, strongly suggesting these are false positives (about six would be expected from the success rate for the 56 fossils tested). Conversely, we retrieved *Hadrocodium* as false negative. Although false predictions are expected to be uncommon, several reasons could lead to a deviation of the TMI from the distribution expected for the thermal regime. These include errors pertaining to the segmentation and measurement of semicircular canals and skulls, but can also reflect major behavioural deviations (e.g., *Zaglossus*⁴⁸), important changes in the relationships between the membranous and bony labyrinths (e.g., Phocidae⁴⁹), and unique modifications in the composition of the endolymph (e.g., pleuronectids³²). However, *Thrinaxodon* (n= 2) may represent a true exception, as independent sources of information suggest it may have been endothermic^{12,50}. If this was the case, it would have been an early, independent experiment unrelated to the emergence of mammalian endothermy.

In terms of evolutionary tempo, our results do not support a gradual or multiphasic origin of mammal-like endothermy, but a single abrupt shift (Fig. 4). Indeed, from the Carboniferous to the Middle Triassic, the TMI of non-mammalianomorph synapsids did not significantly deviate from the average value observed in typical ectotherms, such as lepidosaurs. Mammalianomorpha originated ~233 million years ago, during the Carnian Pluvial Episode, an ephemeral period with humid pulses that was marked by elevated climatic instability and relatively low atmospheric oxygen levels^{37,38}. Whether this event played a major role in the emergence of mammalian endothermy is uncertain. However, early dinosaurs, which were potentially

endothermic as well, originated during the same period³⁹. It is plausible that the Carnian Pluvial Episode could have been a shared environmental trigger for the origin of endothermy in these two distantly related clades.

The unmistakable morphology of the mammalian inner ear provides robust clues to the origin of endothermy. The evolution of smaller, thinner semicircular ducts of the mammalian inner ear in response to the acquisition of endothermy and increased activity, coincided with a crucial pulse in the emergence of the mammalian *bauplan*, including proportionally large brains and body miniaturization. Endothermy and concomitant increase of activity levels were decisive in the Mesozoic evolutionary radiation of mammals and their subsequent major ecological expansion during the Cenozoic.

Methods

Comparative inner ear sample

Three inner ear samples were analysed referred to as the 3D bony, 3D membranous and 2D membranous samples, comprising 341 species (Supplementary Methods). The 3D bony sample consists of 3D endocasts of bony semicircular canals (SC) of 234 extant species [7 amphibians, 67 lepidosaurs (69 specimens), 6 turtles, 9 crocodylians, 72 birds, 73 mammals], and 64 extinct species [1 diadectomorph, 3 non-saurian reptiles, 1 archosauromorph, 2 non-therapsid synapsids, 5 non-neotherapsid therapsids (6 specimens), 16 anomodonts (19 specimens), 5 gorgonopsians, 6 therocephalians (7 specimens), 9 non-probainognathian cynodonts (11 specimens), 3 non-mammaliomorph probainognathians, 9 non-mammalian mammaliomorphs (11 specimens), 4 mammals]. We used non-synapsid fossils to test the method outside the clade of interest at deep divergence time points. The 3D membranous sample consists of 3D endocasts of membranous semicircular ducts (SD) of 50 extant species (1 crocodylian, 9 birds, 3 lepidosaurs, 1 turtle⁵¹, 30 mammals, 3 amphibians⁵², 3 fishes⁵³⁻⁵⁵) Except for fishes, the corresponding bony endocasts of these specimens are part of the 3D bony sample. The 2D membranous sample consists of published photographs⁵⁶⁻⁶¹ and measurements³⁶ of membranous labyrinths of 40 extant fish species (19 chondrichthyans, 21 actinopterygians). The lists of specimens and measurements are provided in Supplementary Data 2.

Data acquisition and processing

The SC endocasts in the 3D bony sample were downloaded from MorphoSource.org or segmented using Amira 5.3.3 (Visage Imaging Inc. & Konrad-Zuse-Zentrum, Berlin, Germany) from existing and new computed tomography (CT) images obtained with μ CT, or propagation phase-contrast synchrotron microtomography (Extended Data Fig. 1). Segmentation was done based on the contrast between bone and air for extant specimens, but manually for fossils. A wax endocast model of *Dimetrodon* sp. (FMNH PR 4976) was digitized using photogrammetry (Supplementary Note 1). The endocasts of SDs and SCs in the 3D membranous sample were segmented from μ CT scans of the ear region of extant specimens, acquired from autopsies or museum collections and prepared as described previously²⁷. Segmentation

and additional processing²⁷ was done in Avizo 7.1 (Visualization Science Group, Burlington, USA) and Geomagic Studio 12 (Raindrop Geomagic Inc, Morrisville, USA). Further information about the specimens and scans are given in Supplementary Data 3.

Measurements of 3D specimens

Four linear measurements were taken per SC for all specimens in the 3D bony and membranous samples: two-dimensional length of the slender portion²⁷, cross-sectional diameter, and major and minor axes of each SC (Extended Data Fig. 2). These functionally relevant measurements mirror SD metrics and were designed to be expedite. The length of the slender portion is taken on the SD midline, which is closer to the outermost wall of the SC^{27,62,63}, from the ampullar junction of the SD to the common crus or vestibule (Extended Data Fig. 2). The distal part of the slender portion of the lateral canal is often fused with the vestibule, especially in ectothermic taxa, and ends at the common crus wall. The major and minor axes are taken perpendicular to each other, following the ellipse that best fits the SD torus. They do not follow anatomical landmarks but their endpoints are placed on the SD midline (Extended Data Fig. 2). The radius of curvature and eccentricity of each SC torus was calculated from the semi-minor and semi-major axes, respectively taken as half the measured minor and major axes (Supplementary Methods). Measurements were taken five times and averaged to reduce error. Measurements of major and minor axes of the SC were taken using the 'straight line' tool of ImageJ⁶⁴, on scaled screenshots from Amira or Avizo, where the screen plane was aligned to the plane of each SC. Measurement of lengths of slender portions²⁷ were taken on the same screenshots, using the 'segmented line' tool of ImageJ. SC planes were approximated visually before taking screenshots. A comparison with a more accurate method, which use landmarks placed along each canal to find the best fitting SC planes, was made in XLSTAT 2018.1.1⁶⁵; no significant differences were found (paired Student t-test, N = 6, P = [0.054 – 0.93], two tailed). The cross-sectional diameter of each SC was measured in Amira, using the 'SurfaceThickness' tool, by selecting five distant points along the slender portion of the SC perpendicular to its plane and averaging their values (Extended Data Fig. 2). Cross-sectional diameters of problematic fossil specimens (e.g., showing obvious segmentation artefacts) were measured using the 'straight line' tool of ImageJ, on scaled screenshots where the plane of the SC was placed parallel to the screen plane. Seven fossil specimens (FMNH UR 161, BPI/1/375, MCZ 1161, GPIT/RE/7119, NHCC LB631, NHCC LB178, NHCC LB387) had incomplete SCs. We estimated missing measurements of these specimens in R v.4.0.3⁶⁶ with pls 2.7-3⁶⁷, using cross-validated partial least-square regressions on a set of 281 species with all measurements (Supplementary Data 2). Reproducibility was assessed in XLSTAT 2018.1.1 by comparing measurements taken by R.A. and R.D. on a subsample of 77 specimens. All 12 variables are left-skewed, and a two-tailed Kolmogorov-Smirnov showed no significant difference, p-value=[0.404-1.000]. Repeatability was tested by comparing measurements taken by R.A. and shows no significant intraobserver variation (repeatability scoring between 2.14 to 8.67%; signal to noise ratio minimum of 16.254 where >5 is considered adequate, Supplementary Data 4).

Morphological and functional analyses of the 3D membranous sample were performed using Ariadne Toolbox²⁷. Input data included surfaces and linesets representing individual components of the duct system (e.g., slender parts and ampullae, modelled cupulae²⁷). The average height of each cilia area was measured on the μ CT scans. Endolymph density was taken as 1000 kg.m^{-3} , Poisson ratio as 0.48 and cupula shear modulus as 1.44 Pa^{27} . Output parameters included, among others, wall shape drag factor, three-dimensional length and cross-sectional area of the slender portion of each SD, enclosed area of the projection of each SD torus on its maximal response plane, and a transfer factor linking endolymph volume displacement to cilia deflection (deflection factor hereafter). Deflection factors of published specimens⁵¹⁻⁵⁵ were estimated from average cupula thickness and cross-sectional area of the ampulla above the crista, following allometric regressions (Supplementary Note 2).

Measurements of 2D images

The 2D membranous sample consists of published photographs⁵⁶⁻⁶¹ and measurements³⁶ of membranous labyrinths. We used ImageJ to process photographs and measure areas enclosed by SD torii, major and minor axes, lengths of slender portions, and inner duct radii (Supplementary Data 2). Photographs were generally taken in lateral view and show the planes of the anterior and posterior SDs at an angle, projected onto the sagittal plane. The resulting distortion can be corrected by multiplying the horizontal axis of the image by $1/\cosine$ of the angle of a specific duct, providing a good representation of undistorted size and shape. Where available, the angles of the planes of the anterior and posterior ducts to the sagittal plane were measured in superior view. For specimens without a superior view, we generally used an angle of 45° to undistort the views (Supplementary Data 2). The undistorted views of the anterior and posterior ducts were used to measure corresponding SDs. When a superior view was available, measurements for the lateral SD were done on this view. For specimens without a superior view, the maximum distance measured between any points on the lateral semicircular duct in lateral view was taken as its major axis. Missing measurements were estimated in R, using cross-validated partial least-square regressions on a set with all measurements (Supplementary Data 2). Cross-sectional radii of bony canals were predicted from outer duct thickness, using allometric regressions (Supplementary Note 2).

Body temperature, body size and phylogeny

Body temperatures of extant species were obtained from the literature (Supplementary Data 2), supplemented by Traitbank (<https://eol.org/traitbank>). For ectothermic taxa, preferred body temperatures were chosen. When both activity range and preferred range of body temperatures were provided, we took the average of the latter. In a few instances (11 ectotherm species) we used online pet care information to estimate preferred body temperature. Values for fish species were obtained from FishBase (<http://www.fishbase.org>).

Three body size variables were used: condylobasal length, condylo-anteroorbital length, and square root of body mass. Condylobasal length (posteriormost border of the occipital condyle(s) to the anteriormost tip of the snout, projected onto the sagittal plane) was used to represent cranial size and could be measured for most specimens (Supplementary Data 2). To avoid bias introduced by snout lengths that are either exceptionally long (e.g., gharials) or short (e.g., anomodonts), we defined the condylo-anteroorbital length as the linear distance from the posteriormost border of the occipital condyle(s) to the anteriormost border of the orbit, projected onto the sagittal plane (see measurements in Supplementary Data 2). The body mass was measured whenever possible (Supplementary Data 2). We used typical adult values rather than extremes, and male and female values were averaged for sexually dimorphic species. For fossils and some specimens of the 3D bony sample, body mass was predicted using an allometric multiple regression of body mass and condylobasal and condylo-anteroorbital lengths (Supplementary Note 2). Predictions were refined by computing phylogenetically informed body mass residuals.

The phylogeny used in this study (Supplementary Data 5) was built in Mesquite 3.5⁶⁸, using relationships and divergence dates between extant taxa provided by TimeTree⁶⁹ (<http://www.timetree.org>) as a backbone to which extinct clades and species were connected. Relationships at the level of Neoaves were modified from TimeTree to fit assumptions of other published accounts^{70,71}. Relationships and divergence dates of actinopterygians and chondrichthyans that were not covered by TimeTree were obtained from the literature⁷²⁻⁷⁴. The reasoning behind phylogenetic relationships, divergence dates and last occurrence data is detailed in Supplementary Note 3 and follow best practices⁷⁵.

Defining the Thermo-Motility Index

Following a single duct model, we characterize aspects of semicircular duct biomechanics using two parameters: the upper corner frequency, which limit the high frequency head motion optimally detected by the SD, and the gain to angular velocity, which determines sensitivity. The upper corner frequency and sensitivity of a SD can be expressed as^{26,27}:

$$\omega_{2,n} \approx \frac{\mu_{(T)} \lambda_{\mu S,n}}{2\rho\pi \cdot a_{s,n}} \text{ (Equ. 1) and } G_{V,n} \approx \frac{2\rho\Lambda_n E_n a_{s,n}^2}{\mu_{(T)} \lambda_{\mu S,n} L_{S,n}} \text{ (Equ. 2)}$$

where ω_2 is the upper corner frequency of the SD n (i.e., anterior, posterior and lateral); G_V corresponds to its sensitivity; $\mu_{(T)}$ is endolymph viscosity at temperature T ; ρ is its density ($1000\text{kg}\cdot\text{m}^{-3}$); $\lambda_{\mu S}$ and a_S are the average wall shape drag factor and average cross-sectional area of the slender portion of the SD, respectively; Λ is the enclosed area of the projection of the SD torus on its maximal response plane; E is the deflection factor; and L_S is the three-dimensional length of the slender portion of the SD (Supplementary Methods). As body size increases, upper corner frequencies of the SDs decrease while their sensitivities increase³⁶, reflecting adaptations to more sluggish head motion. Similarly, as head

motion becomes more vigorous (e.g., increased activity), increased upper corner frequencies and decreased sensitivities are predicted.

The aim of this study is to predict the thermal regime of extinct synapsids. Equ. 1 and 2 denote that increasing body temperature, as seen in endotherms, decrease upper corner frequencies and increase sensitivities of SDs, through endolymph viscosity. This would lead to degraded semicircular duct function if not compensated for, through morphological or physico-chemical adaptation of the SDs. Furthermore, as endotherms are more active³⁴ (Supplementary Data 1), and show more vigorous head motion, they need even higher upper corner frequencies and lower sensitivities, leading to further SD adaptation. Tracking these SD adaptations thus offers an opportunity to assess the thermal regime of an organism, given its body size.

We re-expressed SD function to introduce the Thermo-Motility Index (TMI), which is positively related to body temperature and head motion and can be used to infer the thermal regime of an extinct organism. The TMI was designed to maximize membranous labyrinth information derived from preserved bony canals and facilitate comparisons of specimens of different body sizes (Supplementary Methods), because extinct organisms do not retain morphological information from the membranous labyrinth:

$$TMI_{P,n,Z} \approx I_{B,P,n,Z} + I_{M,P,n} + I_E \approx \left(f(K_{H,Z}) + \varepsilon_{PK_{H,n,Z}} \right) - \left(\frac{C_{T_1}}{T + C_{T_2}} \right) + C_{P,n,Z} \quad (\text{Equ. 3})$$

I_B , I_M and I_E are the bony, membranous-only and endolymph parts of the TMI, respectively; P is either the upper corner frequency or sensitivity of the SD n and Z correspond to the body size variable; $f(K_{H,Z})$ is a function that positively correlates to overall head motion K_H relative to body size and reflects behavioural activity (Supplementary Methods); $C_{P,n,Z}$, C_{T_1} and C_{T_2} are constants; and ε is an error term reflecting the difference between SD function and head motion metrics.

Equ. 3 predicts that endotherms, which show higher body temperature, behavioural activity and overall head motion than ectotherms, will also have a higher TMI. Note from equation 3 that $n \times P \times Z$ different TMIs can be computed, eighteen in the case of this study, representing all possible combinations of the anterior, posterior and lateral upper corner frequencies and sensitivities, and the three body size variables. These TMIs differ slightly but show similar patterns overall (Extended Data Fig. 5, Supplementary Data 2).

The bony part of the TMI

The bony part of the TMI maximizes functional information that can be obtained from bony canals while controlling for body size, and can be expressed as one of two equations, depending on whether the upper corner frequency or the sensitivity is considered (Equ. SM65 and 66 in Supplementary Methods). Variables of these equations correspond to the two-dimensional length and cross-sectional radius of the slender portion of a SC, both expressed relative to its radius of curvature; the radius of curvature of the

SC, expressed relative to each body size variable; and the eccentricity of the SC torus. The radius of curvature was chosen as a scaling variable to isolate the effect of size and provide insight into the functional impact of the shape of the slender portion (relative length and thickness).

The membranous-only part of the TMI

The membranous-only part of the TMI corresponds to functional information measured from SDs that cannot be measured or estimated from bony SCs. It can be expressed as one of two equations, depending on whether upper corner frequency or sensitivity is considered (Equ. SM67 and 68 in Supplementary Methods). Variables of these equations correspond to the cross-sectional area of the slender portion of a SD, expressed relative to the radius of curvature and thickness of the slender portion of corresponding SC; the deflection factor of the cupula, expressed relative to the radius of curvature of corresponding SC; the wall shape drag factor; and two error terms, respectively relating the enclosed area of the SC and the length of its slender portion to corresponding measurements on the SD. Using measured variables, six different versions of the membranous-only part of the TMI were computed for each species in the 3D and 2D membranous sets. Then, for each specimen in the 3D bony set, the membranous-only part was predicted using values computed for the 3D membranous set, weighted according to phylogenetic relatedness.

The endolymph part of the TMI

The endolymph part of the TMI is related to endolymph viscosity through Eq. SM54 and 64 (Supplementary Methods). Data on endolymph viscosity at a given temperature has only been published for eight species (1 bird, 2 mammals, 5 euteleosts)^{32,42,76-81}. Using published data, and these equations, we computed the endolymph parts for these species and found that, except for *Columba livia* and *Pleuronectes platessa*, they have low endolymph viscosity, close to that of water (Extended Data Fig. 4). The phylogenetic distribution of the endolymph part in available species indicates that low-viscosity endolymph was the basal condition for Euarchontoglires and Euteleostei, thus parsimoniously the basal condition for Osteichthyes too. This phylogenetic context allows us to assume *a priori* that the endolymph part of synapsid species did not differ from the basal condition. Following these observations, a low-viscosity endolymph part was chosen for all species analysed in this study except birds and pleuronectids. For non-avian diapsids, amphibians and chondrichthyans, theoretical and empirical relationships between the TMI and body temperature are consistent suggesting, *a posteriori*, the retention of low-viscosity endolymph in these taxa (Fig. 2).

Statistical analyses

Computation of TMIs and statistical analyses were done in R using packages phytools 0.7-70⁸², caper 1.0.1⁸³, geiger 2.0.7⁸⁴, phangorn 2.5.5⁸⁵, Rfast 2.0.1⁸⁶, phylogram 2.1.0⁸⁷ and ape 5.5⁸⁸. P-values were corrected by controlling the false discovery rate (fdr method).

Akaike weights were used for model averaging, and were obtained for each combination by regressing the body temperature ratio (Equ. 3) onto the TMI (Supplementary Note 2, Extended Data Fig. 5). To assess correlations between morphological parameters of SCs and the weighted TMI, we first computed raw averages of the relative canal thickness, the relative slender length, the relative radius of curvature and the eccentricity of the three SCs. We then computed phylogenetic contrasts of the weighted TMI and these average morphological parameters, and calculated Spearman correlations between them (Extended Data Table 1).

Logistic and phylogenetic logistic regressions were fitted to predict the thermoregulatory regime of extant amniote specimens from their weighted TMI (Supplementary Note 2). Resulting logistic regressions were used to predict probabilities of endothermy for each node of the tree and each fossil species, using corresponding weighted TMI (Fig. 3, Extended Data Fig. 6, Extended Data Table 2, 3). Weighted TMI of each node of the phylogenetic tree were obtained by maximum likelihood reconstruction of ancestral states under Brownian motion, using weighted TMI of all tips. Accuracy of predictions was assessed one hundred times by randomly selecting 151 extant species, fitting a logistic regression to predict their thermoregulatory regime from their weighted TMI, using the fitted logistic regression to predict the thermoregulatory regime of 75 extant species that were not used to produce the logistic regression, and comparing outcomes with real thermoregulatory regimes. An endothermic regime was predicted for a probability higher than 0.5 in these tests.

Declarations

Data availability

The raw datasets used in this study are available at [doi pending publication; dataset is available for reviewers in Final R DATA.zip].

Code availability

The R scripts used in this study are available at [doi pending publication; dataset is available for reviewers in Final R DATA.zip].

Acknowledgements

Funding for this project was provided by the Fundação para a Ciência e a Tecnologia postdoctoral fellowship SFRH/BPD/96205/2013, FCT - AGA KHAN Development Network grant number 333206718, National Geographic Society grant number CP-109R-17, the Field Museum, NSF EAR-1337291, the Max Planck Society and the Calleva Foundation. We acknowledge intellectual contributions from discussions with R. Rabbitt. We would like to thank J. White, S. Walsh, P. Campbell, S. Pierce, C. Capobianco, S. Chapman, J. D. Cundiff, A. Wynn, P. Gill, E. Rayfield, J. Hopson, R. Asher, A. Isch, W. Simpson, A. Stroup, A. Resetar, J. Mata, J.-J. Hublin, D. Plotzki, H. Temming, W. van Gestel, J. Jansen, R. Allain, S. W. Evers, M. J. Mason, P.-O. Antoine and A. Schmitt. We also thank the Institute of Veterinary Pathology and the

Veterinary Clinic for Birds and Reptiles at Leipzig University, the Leibniz Institute for Zoo and Wildlife Research and the German Primate Center at Göttingen. We acknowledge the MRI platform member of the national infrastructure France-BioImaging supported by the French National Research Agency (ANR-10-INBS-04, «Investments for the future»), the labex CEMEB (ANR-10-LABX-0004) and NUMEV (ANR-10-LABX-0020). Some silhouettes were obtained from Phylopic.org.

Author contributions

RA, RD and KDA designed the study and interpreted the data. RA and RD collected and analysed the data and wrote the manuscript, with inputs by FS, KDA and PMB. RD developed the Thermo-Motility Index and wrote the code. KDA and RA reviewed time divergence dates and last occurrence data. RD, FS and AS collected specimens for membranous labyrinth analysis. All authors contributed raw and/or processed data, discussed the results and commented on the draft manuscript.

Competing interest declaration

The authors declare no competing interests.

Additional information

Information is available for this paper.

Correspondence and requests for materials should be addressed to Ricardo Araújo (Ricardo.araujo@tecnico.ulisboa.pt), Romain David (r.david@nhm.ac.uk), and Kenneth D. Angielczyk (kangielczyk@fieldmuseum.org).

Reprints and permissions information is available at www.nature.com/reprints.

References

1. Lovegrove, B. G. A phenology of the evolution of endothermy in birds and mammals. *Biol. Rev.* **92**, 1213–1240 (2017).
2. Lovegrove, B. G. *Fires of Life: Endothermy in Birds and Mammals* (Yale Univ. Press, 2019).
3. Benton, M. J. in press. The origin of endothermy in synapsids and archosaurs and arms races in the Triassic. *Gondwana Res.*
4. Charig, A. J. in *Studies in Vertebrate Evolution* (eds. Joysey, K.A. & Kemp, T.S.) 121–155 (Oliver & Boyd, 1972).
5. Kubo, T. & Benton, M. J. Tetrapod postural shift estimated from Permian and Triassic trackways. *Palaeontology* **52**, 1029–1037 (2009).
6. Smith, R. M. H. & Botha-Brink, J. Morphology and composition of bone-bearing coprolites from the Late Permian Beaufort Group, Karoo Basin, South Africa. *Palaeogeogr. Palaeoclimatol. Palaeoecol.* **312**, 40–53 (2011).

7. Huttenlocker, A. K. & Farmer, C. G. Bone microvasculature tracks red blood cell size diminution in Triassic mammal and dinosaur forerunners. *Curr. Biol.* **27**, 48–54 (2017).
8. Jones, K. E., Angielczyk, K. D. & Pierce, S. E. Stepwise shifts underlie evolutionary trends in morphological complexity of the mammalian vertebral column. *Nature Comm.* **10**, 5071 (2019).
9. Benoit, J. et al. Endocranial casts of pre-mammalian therapsids reveal an unexpected neurological diversity at the deep evolutionary root of mammals. *Brain, Behav. Evol.* **90**, 311–333 (2017).
10. Bennett, A. F. & Ruben, J. A. in *The ecology and biology of mammal-like reptiles* (eds. Hotton III N., MacLean P. D., Roth, J. J., Roth, E. C.) 207–218 (Smithsonian Institution Press, 1986).
11. Brink A.S. Speculation on some advanced mammalian characteristics in the higher mammal-like reptiles *Paleontol. Afr.* **4**, 77–96 (1957).
12. Ray, S., Botha, J. & Chinsamy, A. Bone histology and growth patterns of some nonmammalian therapsids. *J. Vertebr. Paleontol.* **24**, 634-648 (2004).
13. Faure-Brac, M. G. & Cubo, J. Were the synapsids primitively endotherms? A palaeohistological approach using phylogenetic eigenvector maps. *Phil. Trans. R. Soc. B*, **375**, 20190138 (2020).
14. Bajdek, P. et al. Microbiota and food residues including possible evidence of pre-mammalian hair in Upper Permian coprolites from Russia. *Lethaia* **49**, 455–477 (2016).
15. Farmer, C.G. Parental care, destabilizing selection, and the evolution of tetrapod endothermy. *Physiology* **35**, 160–176 (2020).
16. Rey, K. et al. Oxygen isotopes suggest elevated thermometabolism within multiple Permo-Triassic therapsid clades. *eLife* **6**, e28589 (2017).
17. Newham, E. et al. Reptile-like physiology in Early Jurassic stem-mammals. *Nature Comm.* **11**, 5121 (2020).
18. Angielczyk, K. D. & Schmitz, L. Nocturnality in synapsids predates the origin of mammals by over 100 million years. *Proc. R. Soc. B* **281**, 20141642 (2014).
19. Rowe, T. B., Macrini, T. E. & Luo, Z.-X. Fossil evidence on origin of the mammalian brain. *Science* **332**, 955–957 (2011).
20. Crompton, A. W. et al. Structure of the nasal region of non-mammalian cynodonts and mammaliaforms: speculations on the evolution of mammalian endothermy. *J. Vertebr. Paleontol.* **37**, e1269116 (2017).
21. Benoit, J. et al. The sixth sense in mammalian forerunners: Variability of the parietal foramen and the evolution of the pineal eye in South African Permo-Triassic eutheriodont therapsids. *Acta Palaeontol. Pol.* **61**, 777–789 (2016).
22. Benoit, J., Manger, P. R. & Rubidge, B. S. Palaeoneurological clues to the evolution of defining mammalian soft tissue traits. *Sci. Rep.* **6**, 25604 (2016).
23. Botha-Brink, J., Soares, M. B. & Martinelli, A. G. Osteohistology of Late Triassic prozostrodontian cynodonts from Brazil. *PeerJ* **6**, e5029 (2018).

24. Lambertz, M., et al. Caseian point for the evolution of a diaphragm homologue among the earliest synapsids. *Ann. N. Y. Acad. Sci.* **1385**, 3–20 (2016).
25. Owerkowicz, T. et al. in *Great Transformations in Vertebrate Evolution* (eds. Dial, K. P., Shubin N., Brainerd, E. L.) 143–165 (University of Chicago Press, 2015).
26. Rabbitt, R. D., Damiano, E. R. & Grant, J. W. in *The vestibular system* (eds Highstein, S. M. et al) 153–201 (Springer, 2004).
27. David, R. et al. Assessing morphology and function of the semicircular duct system: introducing new in-situ visualization and software toolbox. *Sci. Rep.* **6**, 1-14 (2016).
28. Highstein, S. M., Fay, R. R. & Popper, A. N. *The Vestibular System* (Springer, 2004).
29. Fitzpatrick, R. C., Butler, J. E. & Day, B. L. Resolving head rotation for human bipedalism. *Curr. Biol.* **16**, 1509–1514 (2006).
30. Berthoz, A. in *Brain and space* (ed. Paillard, J.) 81–111 (Oxford University Press, 1991).
31. Angelaki, D. E. & Cullen, K. E. Vestibular system: The many facets of a multimodal sense. *Annu. Rev. Neurosci.* **31**, 125–150 (2008).
32. Ten Kate, J. H. & Kuiper, J. W. The viscosity of the Pike's endolymph. *J. Exp. Biol.* **53**, 495–500 (1970).
33. Oman, C. M. in *The Vestibular System: Function and Morphology* (ed Gualtierotti, T.) 251–274 (Springer, 1981).
34. Garland, T. & Albuquerque, R. L. Locomotion, energetics, performance, and behavior: a mammalian perspective on lizards, and vice versa. *Integr. Comp. Biol.* **57**, 252-266 (2017).
35. Hirt, M. R. et al. A general scaling law reveals why the largest animals are not the fastest. *Nat. Ecol. Evol.* **1**, 1116–1122 (2017).
36. Jones, G. M., & Spells, K. E. A theoretical and comparative study of the functional dependence of the semicircular canal upon its physical dimensions. *Proc. R. Soc. Lond. B Biol. Sci.* **157**, 403–419 (1963).
37. Dal Corso, J. et al. Carbon isotope records reveal synchronicity between carbon cycle perturbation and the “Carnian Pluvial Event” in the Tethys realm (Late Triassic). *Glob. Planet. Change* **127**, 79–90 (2015).
38. Berner, R.A., Vandenbrooke, J. M. & Ward, P.D. Oxygen and evolution. *Science* **316**, 557–558 (2007).
39. Bernardi, M. et al. Dinosaur diversification linked with the Carnian Pluvial Episode. *Nature Comm.* **9**, 1499 (2018).
40. Grigg, G. C., Beard, L. A. & Augee, M. L. The evolution of endothermy and its diversity in mammals and birds. *Physiol. Biochem. Zool.* **77**, 982–997 (2004).
41. Creath, R. et al. The role of vestibular and somatosensory systems in intersegmental control of upright stance. *J. Vest. Res.* **18**, 39–49 (2008).
42. Money, K. E. et al. Physical properties of fluids and structures of vestibular apparatus of the pigeon. *Am. J. Physiol. Leg. Content* **220**, 140–147 (1971).

43. Nicol, S.C. Energy homeostasis in monotremes. *Front. Neurosci.* **11**, 195 (2017).
44. Jones, K. E. et al. Regionalization of the axial skeleton predates functional adaptation in the forerunners of mammals. *Nature Ecol. Evol.* **4**, 470-478 (2020).
45. Opiang, M. D. Home ranges, movement, and den use in long-beaked echidnas, *Zaglossus bartoni*, from Papua New Guinea. *J. Mammal.* **90**, 340-346 (2009).
46. Spoor, F. & Thewissen, J. G. M. in *Senses on the threshold: adaptations in secondarily aquatic vertebrates* (eds. Thewissen, J. G. M., Nummela, S.). 257–86 (Univ. Calif. Press, 2008).
47. Botha, J. & Chinsamy, A., Growth patterns of *Thrinaxodon liorhinus*, a non-mammalian cynodont from the lower Triassic of South Africa. *Palaeontology* **48**, 385-394 (2005).
51. Evers, S. W. et al. Neurovascular anatomy of the protostegid turtle *Rhinochelys pulchriceps* and comparisons of membranous and endosseous labyrinth shape in an extant turtle. *Zool. J. Linn. Soc.* **187**, 800-828 (2019).
52. Mason, M. J. et al. The frog inner ear: picture perfect? *J. Assoc. Res. Otolaryngol.* **16**, 171-188 (2015).
53. Schulz-Mirbach, T. et al. A unique swim bladder-inner ear connection in a teleost fish revealed by a combined high-resolution microtomographic and three-dimensional histological study. *BMC Biol.* **11**, 1-13 (2013).
54. Schulz-Mirbach, T., Heß, M. & Metscher, B. D. Sensory epithelia of the fish inner ear in 3D: studied with high-resolution contrast enhanced microCT. *Front. Zool.* **10**, 1-11 (2013).
55. Schulz-Mirbach, T., Heß, M. & Plath, M. Inner ear morphology in the Atlantic molly *Poecilia mexicana* –first detailed microanatomical study of the inner ear of a cyprinodontiform species. *PLoS One* **6**, e27734 (2011).
56. Ghanem, T. A., Rabbitt, R. D. & Tresco, P. A. Three-dimensional reconstruction of the membranous vestibular labyrinth in the toadfish, *Opsanus tau*. *Hearing Res.* **124**, 27-43 (1998).
57. Buran, B. N., Deng, X. & Popper, A. N. Structural variation in the inner ears of four deep-sea elopomorph fishes. *J. Morph.* **265**, 215-225 (2005).
58. Deng, X., Wagner, H. J. & Popper, A. N. The inner ear and its coupling to the swim bladder in the deep-sea fish *Antimora rostrata* (Teleostei: Moridae). *Deep Sea Res. Part I: Oceanogr. Res. Pap.* **58**, 27-37 (2011).
59. Deng, X., Wagner, H. J. & Popper, A. N. Interspecific variations of inner ear structure in the deep-sea fish family Melamphaidae. *Anat. Rec.* **296**, 1064-1082 (2013).
60. Evangelista, C. et al. A comparison of the external morphology of the membranous inner ear in elasmobranchs. *J. Morphol.* **271**, 483-495 (2010).
61. Gauldie, R. W., Mulligan, K. & Thompson, R. K. The otoliths of a chimaera, the New Zealand elephant fish *Callorhynchus milii*. *N. Zeal. J. Mar. Freshw. Res.* **21**, 275-280 (1987).
62. Gray, A. A. *The labyrinth of animals: including mammals, birds, reptiles and amphibians. I.* (Churchill, 1907).

63. Gray, A. A. *The labyrinth of animals: including mammals, birds, reptiles and amphibians. II.* (Churchill, 1908).
64. Schneider, C. A., Rasband, W. S. & Eliceiri, K. W. NIH Image to ImageJ: 25 years of image analysis. *Nature Methods* **9**, 671-675 (2012).
65. Addinsoft. XLSTAT statistical and data analysis solution. New York, USA. <https://www.xlstat.com> (2021).
66. R Core Team. R: A language and environment for statistical computing. R Foundation for Statistical Computing, Vienna, Austria. URL <https://www.r-project.org/> (2017).
67. Bjørn-Helge M., Wehrens, R. & Liland, K. H. pls: Partial Least Squares and Principal Component Regression. R package version 2.7-3. <https://CRAN.R-project.org/package=pls> (2020).
68. Maddison, W. P. & D. R. Maddison. Mesquite: a modular system for evolutionary analysis. Version 3.61 <http://www.mesquiteproject.org> (2018).
69. Kumar, S. et al. TimeTree: a resource for timelines, timetrees, and divergence times. *Mol. Biol. Evol.* **34**, 1812-1819 (2017).
70. Prum, R. O. et al. A comprehensive phylogeny of birds (Aves) using targeted next-generation DNA sequencing. *Nature* **526**, 569-573 (2015).
71. Suh, A. et al. Ancient horizontal transfers of retrotransposons between birds and ancestors of human pathogenic nematodes. *Nature Comm.* **7**, 1-9 (2016).
72. Naylor, G. J. P. et al. in *Biology of sharks and their relatives 2* (ed. Carrier, J. C., Musick, J. A., Heithaus, M. R.) 31-56 (2012).
73. Bakke, I. & Steinar J. Characterization of mitochondrial ribosomal RNA genes in gadiformes: sequence variations, secondary structural features, and phylogenetic implications. *Mol. Phylogenetics Evol.* **25**, 87-100 (2002).
74. Bakke, I. & Steinar D. J. Molecular phylogenetics of Gadidae and related Gadiformes based on mitochondrial DNA sequences. *Mar. Biotech.* **7**, 61-69 (2005).
75. Parham, J. F. et al. Best practices for justifying fossil calibrations. *Syst. Biol.* **61**, 346-359 (2012).
76. Steer, R. W. The influence of angular and linear acceleration and thermal stimulation on the human semicircular canal (Massachusetts Institute of Technology, 1967).
77. Rauch, S. Biochemie des Hörorgans (Thieme Verlag, 1964).
78. Ten Doesschate, G. Onderzoekingen gedaan in het Fysiologisch Laboratorium der Utrechtse Hogeschool 5e reeks XIV. De eigenschappen van de endolymph van Beenvisschen. (1914).
79. Money, K. E., Sokoloff, M. & Weaver, R. S. *Specific gravity and viscosity of endolymph and perilymph.* In NASA, Second Symposium on the Role of the Vestibular Organs. Washington, DC: NASA 91-98 (1966).
80. Schnieder, E. A. & Schindler, K. in *Biochemie des Hörorgans* (ed Rauch, S.) 164-168 (Georg Thieme Verlag, 1964).

81. Macdonald, J. A. & Wells, R. M. G. in *Biology of Antarctic fish* (eds di Prisco, G., Maresca, B. & Tota B.) 163-178. (Springer, 1991).
82. Revell, L. J. phytools: An R package for phylogenetic comparative biology (and other things). *Methods Ecol. Evol.* **3**, 217-223 (2012).
83. Orme, D. et al. caper: Comparative Analyses of Phylogenetics and Evolution in R. R package version 1.0.1. <https://CRAN.R-project.org/package=caper> (2018).
84. Pennell, M. W. et al. geiger v2.0: an expanded suite of methods for fitting macroevolutionary models to phylogenetic trees. *Bioinformatics* **30**, 2216-2218 (2014).
85. Schliep, K. P. phangorn: phylogenetic analysis in R. *Bioinformatics* **27**, 592-593 (2011).
86. Papadakis, M. et al. Rfast: A Collection of Efficient and Extremely Fast R Functions. R package version 2.0.1. <https://CRAN.R-project.org/package=Rfast> (2020).
87. Wilkinson S. P. & Davy S. K. phylogram: an R package for phylogenetic analysis with nested lists. *J. Open Source Softw.* **3**, 790 (2018).
88. Paradis E. & Schliep, K. ape 5.0: an environment for modern phylogenetics and evolutionary analyses in R. *Bioinformatics* **35**, 526-528 (2019).

Table

Table 1 | Statistical comparisons of the TMI of synapsid groups.

Group	n	Lepidosaur (n = 67)		Mammals (n = 77)	
		Mann-Whitney U	p-value	Mann-Whitney U	p-value
Non-mammalian mammaliamorphs	9	529	1.12 10⁻³	209	0.08
Non-mammaliamorph probainognathians	3	68	0.38	4	0.01
Non-probainognathian cynodonts	9	328	0.68	46	1.97 10⁻⁴
Therocephalians	6	106	0.08	5	4.15 10⁻⁴
Gorgonopsians	5	115	0.30	10	1.19 10⁻³
Anomodonts	16	325	0.03	28	3.78 10⁻⁸
Non-neotherapsids therapsids	5	120	0.34	10	1.19 10⁻³
Non-therapsid synapsids	2	33	0.30	1	0.03

Significant p-values are in bold and have been corrected by controlling the false discovery rate. The TMI of anomodonts is significantly smaller than that of lepidosaurs.

Figures

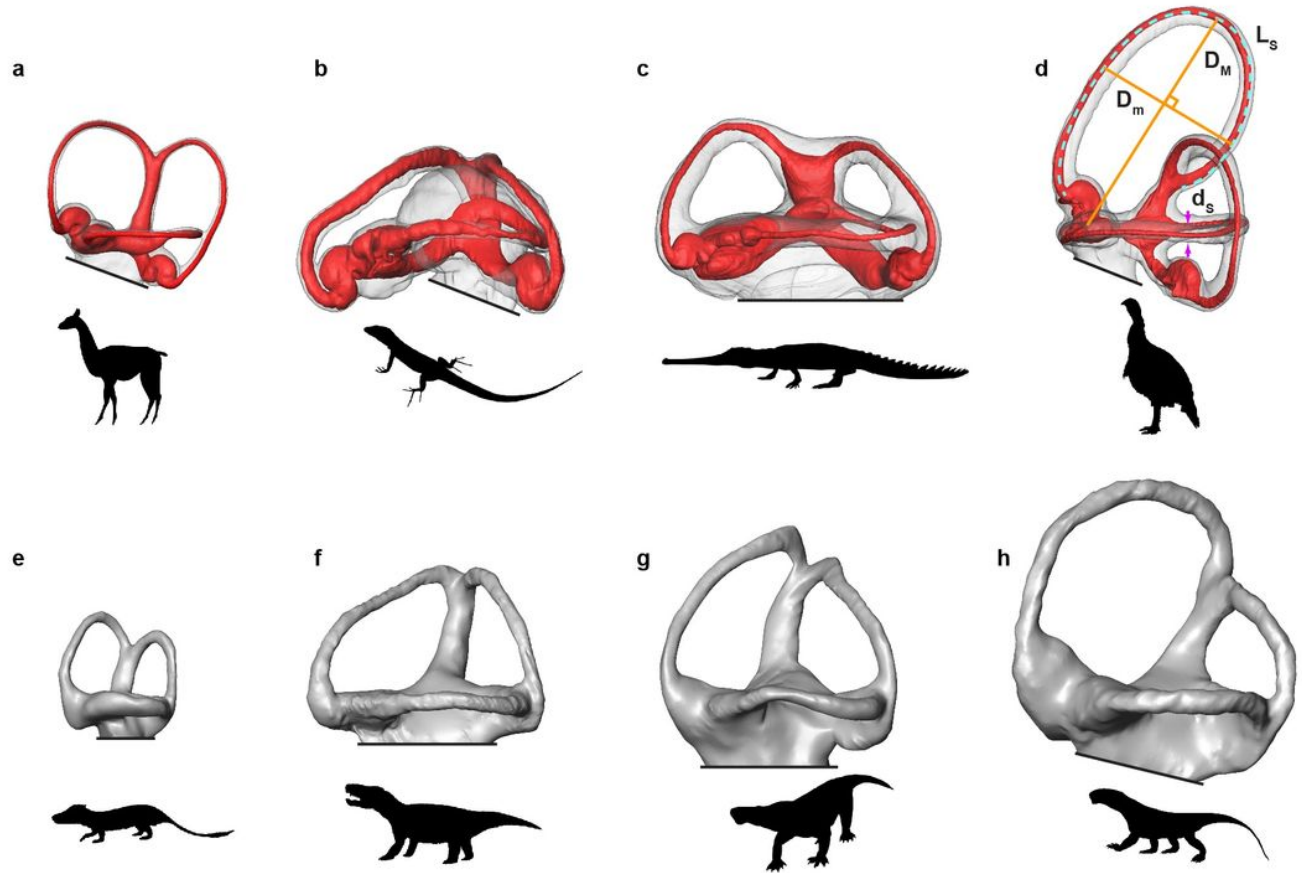


Figure 1

Examples of three-dimensional visualizations of the bony and membranous labyrinths. a-d, Lateral views of the upper part of the bony labyrinth (grey) and the membranous semicircular duct system (red) of an alpaca (a, CEB 130038), a Sicilian wall lizard (b, CEB 130040), a false gharial (c, CEB140070) and a domestic turkey (d, CEB 130069). d, Illustration of measurements of major (D_M) and minor (D_m) axes of the semicircular canal torus, cross-sectional thickness (d_s) and length (L_s) of the slender portion. e-h, Lateral views of the upper part of the bony labyrinth of *Tritylodon* (d, BP/1/4778), *Trirachodon* (e, BP/1/4658), *Microgomphodon* (f, SAM-PK-10160) and *Lemurosaurus* (c, BP/1/816). All labyrinths have been scaled relative to body size, according to the average relative size of the groups.

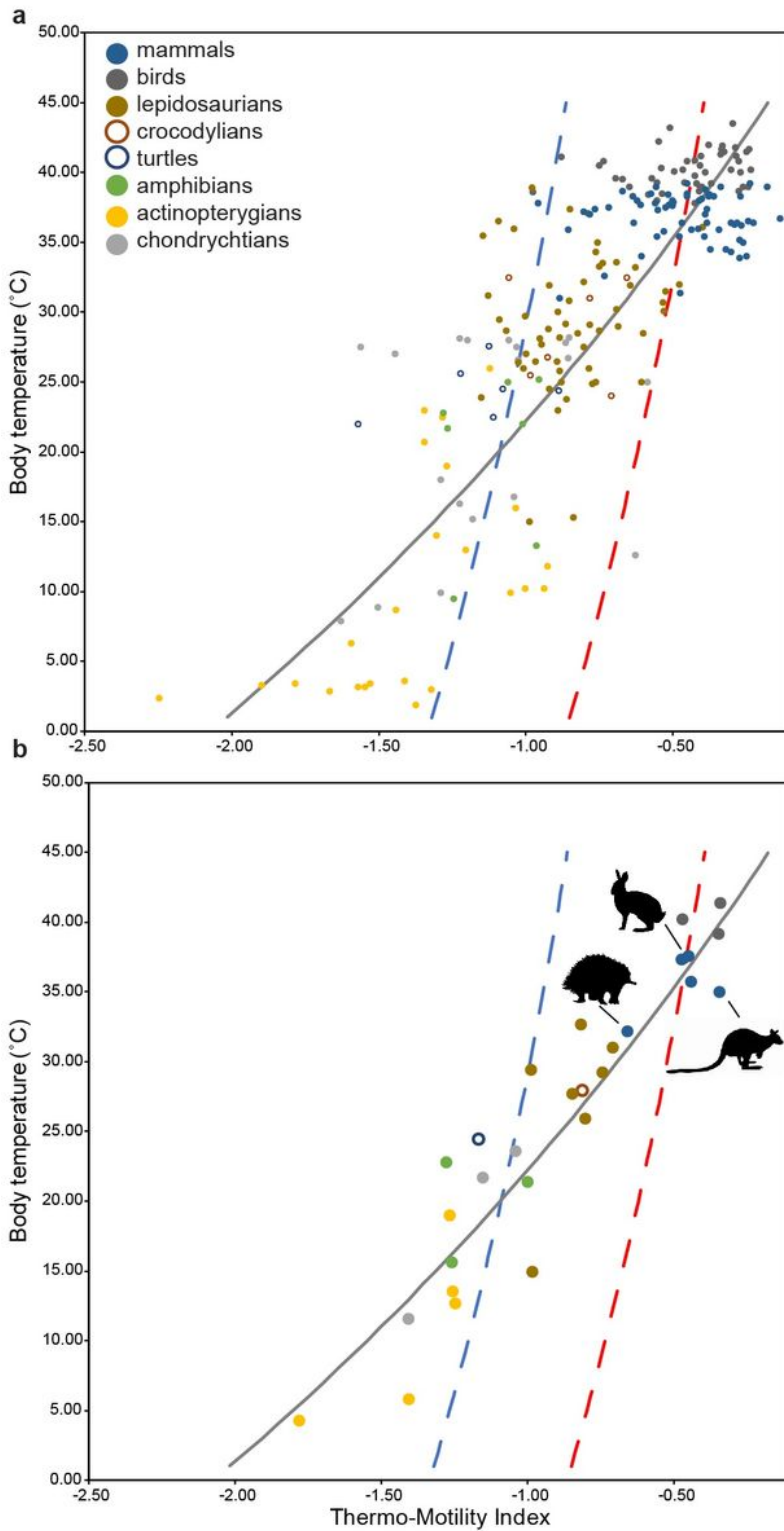


Figure 2

Relationships between the TMI and body temperature. a-b, Scatterplot for individual species (a) and when combined in major groups of vertebrates (b). Dashed curves represent theoretical relationships with body temperature when the TMI only reflect endolymph viscosity for average endotherms (red) and ectotherms (blue). The grey curve represents the empirical relationship for the major groups of vertebrates, taking phylogeny into account. The grey curve deviating from theoretical curves indicates that body temperature

positively affects head motion. Monotremes, euarchontoglires and marsupials are indicated by silhouettes.

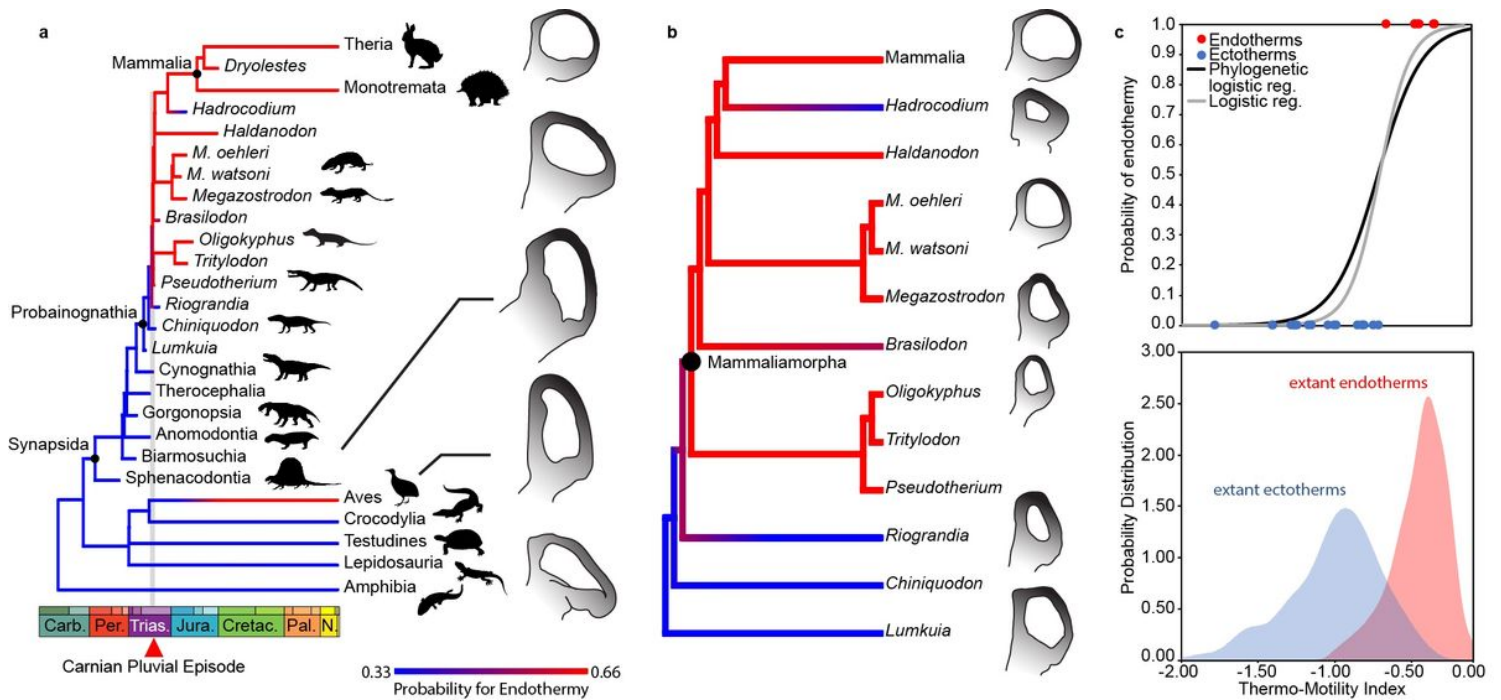


Figure 3

Phylogenetic distribution of the TMI in tetrapods. a-b, Optimization of the TMI onto a time calibrated tree of major tetrapod clades (a), with expanded detail on the cladogram of probainognathians (b). Anterior semicircular canals of example specimens are depicted and scaled to body size. Branch colours reflect the likelihood of being endothermic according to the probability colour scale. The thick grey line (a) represents the uncertainty in the timing of the Carnian Pluvial Episode, which has been exaggerated three times. c, Probability of endothermy calculated from logistic regressions computed from the TMI of extant amniotes (top) and the distribution of the TMI for extant endotherms in red and ectotherms in blue (bottom). Probabilities for major groups of extant vertebrates are shown as dots.

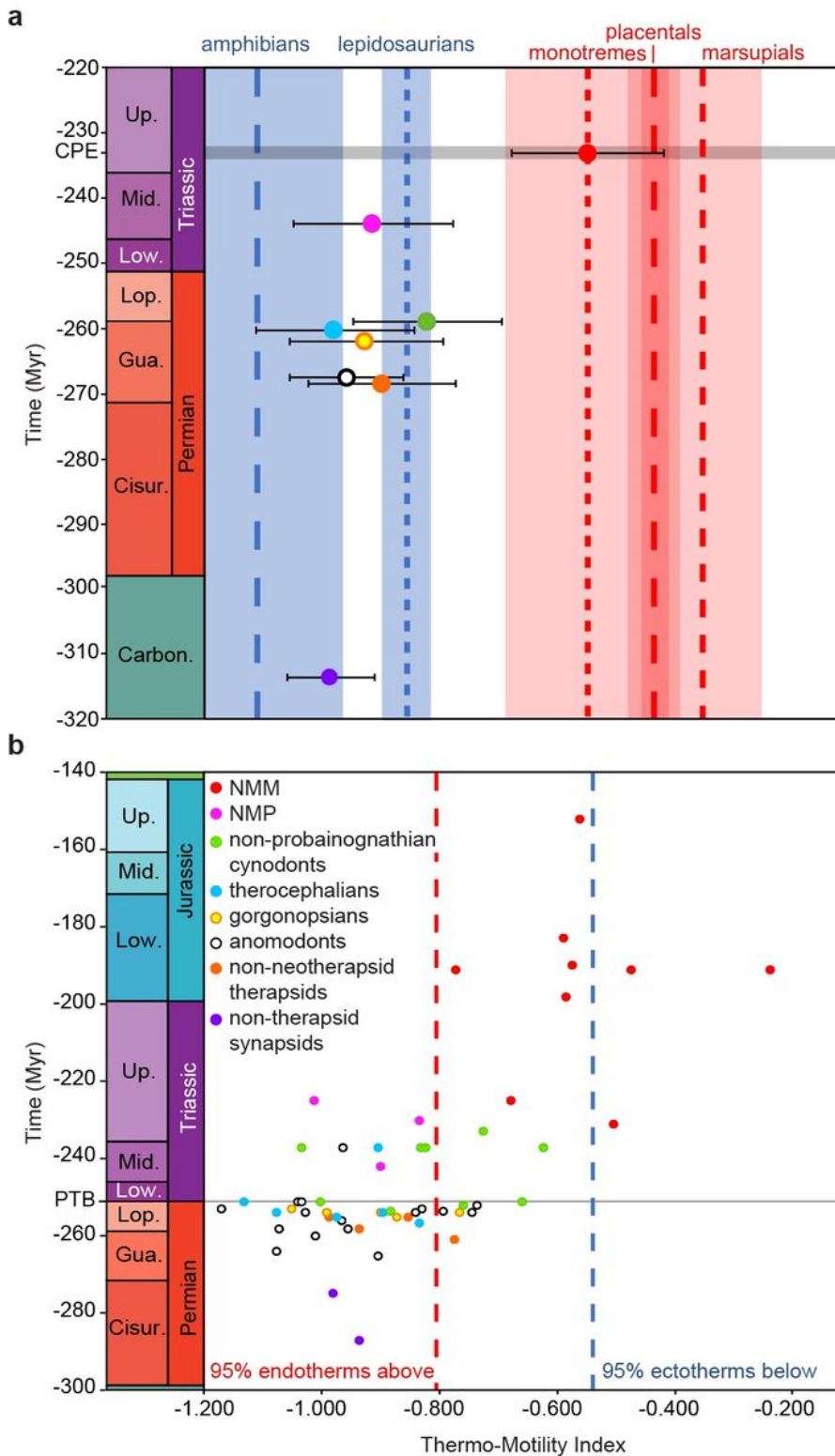


Figure 4

Temporal distribution of the TMI in synapsids. a-b, Scatterplots of geologic time against average TMI for the major groups of fossil synapsids (a) and individual species (b). Geologic age corresponds to the node origin for groups (a) and last appearance datum for species (b). a, Error bars represent the standards error of the mean of the TMI, including variation of the membranous-only part. Dashed lines and shaded areas respectively represent the mean and standard error of the mean of the TMI of example extant endotherm

(red) and ectotherm (blue) clades, excluding specimens outside the 95% confidence interval of these thermal regimes. The thick grey line represents the uncertainty in the timing of the Carnian Pluvial Episode (CPE). b, Dashed lines represent thresholds of the distribution of the TMI of extant endotherms (red) and ectotherms (blue) analysed in this study. The thin grey line represents the Permo-Triassic boundary (PTB).

Supplementary Files

This is a list of supplementary files associated with this preprint. Click to download.

- [SIGuide.doc](#)
- [SupplementaryInformation28052021.pdf](#)
- [SupplementaryData1definitivefinal.xlsx](#)
- [SupplementaryData2definitivefinal.xlsx](#)
- [SupplementaryData3definitivefinal.xlsx](#)
- [SupplementaryData4definitivefinal.xlsx](#)
- [SupplementaryData5definitivefinal.pdf](#)
- [ExtendedData.pdf](#)